

# Wednesday 25 Nov

## PCB Manufacturing and Dimensional Measurement

Free webinar

14.00-16.00 CET | 08.00-10.00 EST

[Register here](#)



Uwe Brand  
Federal Institute of  
Physics & Technology,  
Braunschweig



Markus Fabich,  
Strategic Marketing  
Manager, Olympus



Wiley Analytical Science

**OLYMPUS**

# Thermophysical Properties of an Fe<sub>57.75</sub>Ni<sub>19.25</sub>Mo<sub>10</sub>C<sub>5</sub>B<sub>8</sub> Glass-Forming Alloy Measured in Microgravity

Markus Mohr,\* Douglas C. Hofmann, and Hans-Jörg Fecht


Iron-based metallic glasses are among the lowest-cost form of amorphous metals and have numerous potential applications, such as wear-resistant coatings, cutting tools, and gears. There is an increased interest for using this novel alloys as protective coatings and to produce structural elements by additive manufacturing. If an accelerated process development is desired, computer-based process simulations are nowadays a vital tool. As a consequence, high-quality measurements of the thermophysical properties in the solid and liquid phases are essential for developing numerical simulation models and suitable processing parameters. Due to the high melt reactivity of liquid metals at high temperatures, measurements using conventional containers are challenging, hence containerless methods have to be used. Herein, the thermophysical properties of an Fe-based metallic glass-former have been measured in the liquid phase using the electromagnetic levitator ISS-EML on-board the International Space Station (ISS).

## 1. Introduction

Due to their unique combination of properties, metallic glasses are of particular interest in numerous fields of engineering.<sup>[1]</sup> The much lower material cost, compared with Zr-based metallic glasses,<sup>[2]</sup> together with high corrosion and wear resistance, make Fe-based metallic glasses very attractive for industrial applications.<sup>[3]</sup> Due to the relatively small critical casting thickness of Fe-based metallic glasses (typically below 6 mm), industrial commercialization of Fe-based glass forming alloys are limited to applications such as anticorrosion or thermal-barrier coatings, applied, e.g., by spray coating methods<sup>[3,4]</sup> or laser cladding methods.<sup>[5,6]</sup> The often observed brittleness of Fe-based alloys has driven the development of Fe-based metallic glass compositions with improved ductility and glass-forming ability<sup>[7–9]</sup> and the development of bulk metallic glass matrix composites.<sup>[10–13]</sup>

Dr. M. Mohr, Prof. H.-J. Fecht  
Institute of Functional Nanosystems  
Ulm University  
Albert-Einstein-Allee 47, 89081 Ulm, Germany  
E-mail: markus.mohr@uni-ulm.de

Dr. D. C. Hofmann  
Materials Development and Manufacturing Technology Group  
NASA Jet Propulsion Laboratory  
California Institute of Technology  
Pasadena, CA 91125, USA

 The ORCID identification number(s) for the author(s) of this article can be found under <https://doi.org/10.1002/adem.202001143>.

DOI: 10.1002/adem.202001143

Previously, it was already demonstrated, that by, e.g., powder bed fusion (PBF), thermal spray additive manufacturing (TSAM), and direct energy deposition (DED) of FeCrMoCB a large variety of microstructures can be achieved: fully amorphous, dendrite-reinforced metal matrix composites, and fully crystalline.<sup>[14,15]</sup> Despite these developments, Fe-based metallic glasses have not found widespread use outside of coatings due to their exceptionally low fracture toughness in large glass-forming compositions and their reliance on volatile phosphorous in their tougher compositions. Tough Fe-based metallic glasses have been previously demonstrated in the FeNiBX system, but these are only accessible in the amorphous state through ultrarapid cooling. However, additive manufacturing

of Fe-based metallic glasses will make it possible to realize bulk metallic glass parts from tough Fe-based alloys with low glass-forming ability.

To avoid a time consuming, completely empirical process development for an additive manufacturing process,<sup>[15]</sup> numerical models of the fabrication process have nowadays become an essential instrument. Using the correct simulation models and precise thermophysical property data, the temperature distribution and history, fluid flows in the melt, porosity and other defect formation, as well as the formation of thermal stresses during the solidification in the additive manufacturing process can be predicted.<sup>[16]</sup> In a similar manner, this approach can also be used to improve simulation of other manufacturing processes, such as thermal spraying, laser cladding<sup>[17–20]</sup> and powder production by gas atomization.<sup>[21,22]</sup> Consequently, process simulations based on precise thermophysical properties result in faster process development cycles.

Such numerical simulations need not only to present the correct description of the involved physical phenomena, but they especially require the correct thermophysical properties of the alloy in the solid and liquid phases. While the relevant properties in the solid phase can be measured with commercial measurement equipment, container-based measurement methods for the liquid phase suffer from the high reactivity of liquid metals with the container walls. This can be circumvented by containerless methods, such as electromagnetic levitation.<sup>[23–26]</sup>

The measurements were carried out in the microgravity environment of the international space station ISS. This way, the strong forces necessary to lift the sample in a ground-based electromagnetic levitator are diminished. In microgravity, the much

smaller required positioning field does not heat the sample notably and does also not deform the spherical droplet. That way, a large temperature range above and below the liquidus temperature is accessible. The quiescent conditions allow good temperature control and ensure laminar flow conditions in a large temperature range, which are a prerequisite for the precise determination of the thermophysical properties studied in this work.

We present the containerless measurement of thermophysical properties of liquid  $\text{Fe}_{57.75}\text{Ni}_{19.25}\text{Mo}_{10}\text{C}_5\text{B}_8$  (at%), a new glass-forming metallic glass first reported here, using the ISS-EML on board the European science module “Columbus” of the International Space Station ISS. In this measurement arrangement, the sample can be held in the liquid phase for durations up to about 20 min, whereas parabolic flights can only offer about 20 s of microgravity.<sup>[27]</sup> Only the long duration of microgravity on the International Space Station enables the multitude of measurement methods as presented here.

## 2. Experimental Section

### 2.1. Material

Ingots of  $\text{Fe}_{57.75}\text{Ni}_{19.25}\text{Mo}_{10}\text{C}_5\text{B}_8$  (at%) were produced by melting of the elemental components in an arc-melter in a Ti-gettered high purity Ar atmosphere, followed by multiple re-melting to achieve a homogeneous composition. Pieces of the ingot were then remelted in an arc-melter with subsequent suction casting into a spherical sample of 6.5 mm diameter. After suction casting, the runners and feeders were cut off. The sample surface was then polished and subjected to ultrasonic cleaning in acetone and diethyl ether.

Further pieces of the ingot were used to obtain the liquidus temperature  $T_{\text{liq}}$  and solidus temperature  $T_{\text{sol}}$  of the alloy, as well as the heat of fusion  $\Delta H_f$  using a high-temperature differential scanning calorimeter (DSC). This alloy, which was developed by

NASA JPL/Caltech, is based on the FeNiB eutectic, with small amounts of Mo and C to improve the glass-forming ability. Details about the development of this alloy will be published in the future. However, the glass-forming ability of this alloy was confirmed through splat quenching (see **Figure 1b**). A 1-g sample of  $\text{Fe}_{57.75}\text{Ni}_{19.25}\text{Mo}_{10}\text{C}_5\text{B}_8$  was levitated with an RF-coil and splatted into an approximately 20  $\mu\text{m}$  thick foil (shown in the inset in **Figure 1b**), which was confirmed amorphous via X-ray diffraction.

### 2.2. The ISS-EML Facility

The core element of the electromagnetic levitation facility ISS-EML on board the International Space Station ISS is a coil, which enables the independent heating and positioning of the samples via RF electromagnetic fields.<sup>[28–30]</sup> An axial and a radial high-speed camera are used to observe the sample during processing with a framerate of typically 150 and 200 Hz, respectively. Within the axial camera, a pyrometer is incorporated, which allows the precise measurement of the sample temperature during operation. The spectral emissivity setting of the pyrometer was calibrated using the liquidus temperature obtained by the DSC measurements on ground. The samples are stored in a sample container, which is mounted to the experiment chamber. Using a sophisticated mechanism, the samples can be transported from the sample container to the experiment chamber for the experiments, and back to the sample container. The typical sample size of the 18 samples in the sample chamber is between 6 and 8 mm in diameter each.

**Figure 1a** shows the  $\text{Fe}_{57.75}\text{Ni}_{19.25}\text{Mo}_{10}\text{C}_5\text{B}_8$ -sample levitating in the ISS-EML during processing. The dark shadows visible on the sample origin from the wire cage that is surrounding the sample to confine the sample once the positioning field is switched off. Due to the microgravity conditions, the molten sample forms a near-perfect sphere and has no contact with a container. **Figure 1b**

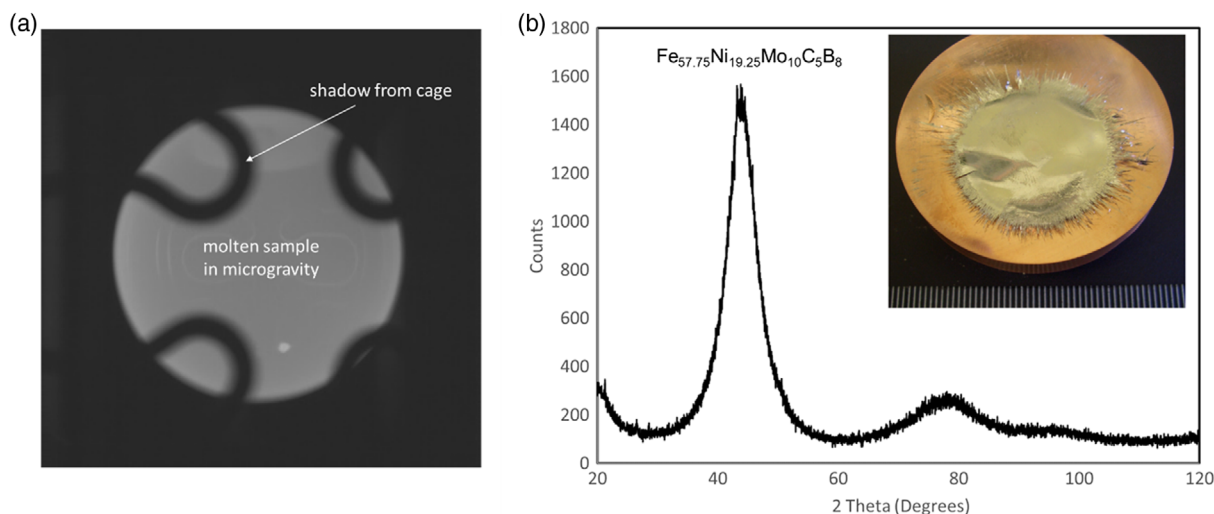


**Figure 1.** a) 6 mm diameter FeNiMoCB sample during microgravity processing on the ISS. The black shadows are the sample cages that confine the samples while it is not processed. b) X-ray diffraction scan from a splat-quench of the same  $\text{Fe}_{57.75}\text{Ni}_{19.25}\text{Mo}_{10}\text{C}_5\text{B}_8$  alloy where the sample was processed containerless, as in (a), but was then rapidly cooled by splatting between copper blocks. The X-ray scan shows the sample to be fully amorphous under the high cooling rate. An image of the splatted sample is shown in the inset after opening the copper blocks.



shows that if the molten sphere from the microgravity experiment were rapidly cooled (at a rate of approximately  $10^6 \text{ K s}^{-1}$ ), the ingot would freeze into the amorphous state.

### 2.3. Surface Tension and Viscosity

The surface tension  $\sigma$  and viscosity  $\eta$  were determined by the oscillating drop method.<sup>[23,25]</sup> Short pulses of the heater field were applied to induce surface oscillations, while the sample shape oscillations were recorded by the two high-speed cameras. Using edge-detection algorithms, the time-dependent projected circumference of the sample was determined and was used to obtain the time-dependent surface oscillation amplitude  $\delta(t)$  and frequency  $f_{\text{osc}}$ . The analyzed relative sample deformations  $\delta(t)/a$  were small enough to prevent the occurrence of nonlinear effects.<sup>[31]</sup> Furthermore, no strong sample rotations were observed, which could also lead to a shift of the oscillation frequency.<sup>[32]</sup> The surface tension  $\sigma$  was calculated by Rayleigh's equation<sup>[33]</sup>

$$\sigma = \frac{3}{8} \pi m f_{\text{osc}}^2 \quad (1)$$

where  $m$  is the sample mass. The internal damping due to the samples viscosity was revealed by the exponential decay of the oscillation amplitude with a time constant  $\tau$ . Using Lambs equation,<sup>[34]</sup> the viscosity was determined by

$$\eta = \frac{3}{20\pi} \frac{m}{a} \frac{1}{\tau} \quad (2)$$

### 2.4. Specific Heat

An alternating current (AC) calorimetry method<sup>[35–38]</sup> is applied to obtain specific heat, thermal conductivity, and total hemispherical emissivity. The method is based on the periodic variation of heating power input  $P(t)$ , which leads to a periodic temperature variation  $T(t)$ . The most convenient way is the modulation of the power input of that form

$$P(t) = P_{\text{av}} + \Delta P \cdot \sin(2\pi f_{\text{mod}} t + \varphi_0) \quad (3)$$

which leads to a temperature signal of the form

$$T(t) = T_{\text{av}} + \Delta T \cdot \sin(2\pi f_{\text{mod}} t + \varphi_1) \quad (4)$$

Then, the heat capacity of the sample can be obtained by

$$C_p = \frac{\Delta P}{2\pi f_{\text{mod}} \Delta T} \cdot f_c(\tau_1, \tau_2, f_{\text{mod}}) \quad (5)$$

where  $f_c(\tau_1, \tau_1, f_{\text{mod}})$  is a correction function that depends on the external and the internal relaxation times  $\tau_1$  and  $\tau_2$ , as well as on the heater modulation frequency.<sup>[35]</sup> With the right choice of the modulation frequency, sample size, etc., the measurement is carried out within the adiabatic regime and  $f_c$  is approximately 1. In the present case, the internal heat relaxation time  $\tau_2$  is small enough to be negligible (about 0.2 s) and only the external heat relaxation time has to be considered in the correction function. A more detailed discussion about the measurement uncertainties involved can be found in the study by Mohr et al.<sup>[39]</sup>

### 2.5. Thermal Conductivity

The cosine of the phase shift  $\varphi = \varphi_0 - \varphi_1$  between the input power and the measured temperature response can be described for the small Biot numbers in this experiment ( $Bi \approx 0.01 \ll 1$ ) as<sup>[38]</sup>

$$\cos(\varphi) = \left( \frac{1}{\tau_1 \tau_2} - \omega_{\text{mod}}^2 \right) \times \left[ \left( \frac{1}{\tau_1 \tau_2} - \omega_{\text{mod}}^2 \right)^2 + \left( \frac{1}{\tau_1} + \frac{1}{\tau_2} \right)^2 \omega_{\text{mod}}^2 \right]^{-\frac{1}{2}} \quad (6)$$

where  $\omega_{\text{mod}} = 2\pi f_{\text{mod}}$  is the angular modulation frequency. By measuring the phase shift  $\varphi$  and the external relaxation time  $\tau_1$ , one can find from Equation (6), the internal relaxation time  $\tau_2$ , by means of a numerical solution procedure. For a spherical geometry of radius  $a$ , the thermal conductivity  $\kappa$  is related with the internal relaxation time  $\tau_2$  by<sup>[35]</sup>

$$\kappa = \frac{3C_p}{4\pi^3 \tau_2 a} \quad (7)$$

and this way, the thermal conductivity  $\kappa$  of the sample can be obtained. However, the obtained apparent thermal conductivity  $\kappa_{\text{ap}}$  is a combination of the real thermal conductivity of the material  $\kappa_{\text{real}}$  and the thermal conductivity driven by the mass transport by fluid flow  $\kappa_{\text{flow}}$ .

### 2.6. Total Hemispherical Emissivity

The stepwise rise of the average power  $P_{\text{av}}$  leads to an increase in the average temperature  $T_{\text{av}}$  in the form

$$T_{\text{av}}(t) = \Delta T_{\text{av}} \cdot e^{-\frac{t}{\tau_1}} \quad (8)$$

where the external relaxation time  $\tau_1$  is characterizing the rate of external heat loss of the sample (heat radiation and if applicable heat conduction in the gas atmosphere). As laid out elsewhere, the rate of heat loss in vacuum<sup>[35]</sup> or argon atmosphere,<sup>[39]</sup> characterized by  $\tau_1$  can be used to obtain the total hemispherical emissivity, by applying the proper heat loss model.

### 2.7. Electrical Resistivity and Mass Density

An inductive measurement of the samples electrical resistivity, as well as its mass density was performed, as described in previous studies.<sup>[40]</sup> The impedance of the circuit connected to the power supply, including the heater coils, changes when a sample is placed in the coils. A calibration measurement of the circuit impedance without sample is used to find the impedance of the sample.<sup>[40]</sup> The sample impedance is related to the frequency of the heater RF current  $\omega_{\text{Htr}}$ , the resistivity of the sample  $\rho_e$  and the radius  $a$  of the sample

$$Z_s(\omega_{\text{Htr}}, a, \rho_e) = C_c \cdot \omega_{\text{Htr}} \cdot a^3 \left[ \frac{1}{q} - \frac{1}{q^2} + i \left( \frac{1}{q} - \frac{2}{3} \right) \right] \quad (9)$$

with

$$q(\omega_{\text{Htr}}, a, \rho_e) = a \sqrt{\frac{\mu_0 \omega_{\text{Htr}}}{2\rho_e}} \quad (10)$$

where  $\mu_0$  is the magnetic permeability of free space. Rearrangement of both equations leads to expressions for the electrical resistivity and sample radius.<sup>[40]</sup> The coil constant  $C_c$  was obtained by proper calibration using a known solid Zr sample and comparison with literature values.

### 3. Results

#### 3.1. Surface Tension and Viscosity

As precursor experiment (before sending the sample to the ISS), a parabolic flight campaign was performed, when a sample with the same composition,  $\text{Fe}_{57.75}\text{Ni}_{19.25}\text{Mo}_{10}\text{C}_5\text{B}_8$ , was also processed. The TEMPUS facility, used in the parabolic flight, is technically similar to the ISS-EML, with respect to the electromagnetic coil geometry, pyrometer, and high-speed cameras. However, during the 20 s of microgravity, the sample is in the liquid phase for about 10 s. This way, only a small number of surface tension and viscosity measurements have been obtained in the parabolic flight. The results of the surface tension measurements obtained during processing in the ISS-EML on board the ISS are shown together with the results from the parabolic flight campaign in **Figure 2a**. The viscosity from both measurement campaigns is shown in **Figure 2b**.

In the measured temperature range from 1425 to 1650 K, the obtained viscosity data are well described by an Arrhenius equation of the form  $\eta(T) = \eta_0 \cdot \exp(E_A/k_B T)$ , where  $E_A$  is a characteristic activation energy and  $k_B$  the Boltzmann constant. The fitting parameters are found to be  $E_A = 0.42$  eV,  $\eta_0 = 1.15$  mPa s.

The measurement uncertainty of the surface tension is determined by the accuracy of the surface oscillation frequency determination, as well as the accuracy of the measured sample mass. The sample mass of 1.14 g was measured with an accuracy of  $\pm 0.01$  g. The surface oscillation frequency is determined with an uncertainty of  $\pm 0.05$  Hz. Hence, the given surface tension data points have an uncertainty of  $\pm 1\%$ . The measurement uncertainty of the viscosity is shown by the error bars in

**Figure 2b**. It is determined by the uncertainty of the sample mass, the sample average radius and the uncertainty of the damping time constant. The sample radius was measured with an uncertainty of  $\pm 0.03$  mm, whereas the uncertainty of the damping time constant is assumed to be about  $\pm 0.025$  s.

#### 3.2. Specific Heat Capacity and Total Hemispherical Emissivity

The specific heat capacity in the liquid phase was determined by the aforementioned AC calorimetry method. The results are shown in **Figure 3a**. The measurement uncertainty of the specific heat capacity is determined by the uncertainty of the temperature oscillation amplitude ( $\pm 0.1$  K), the uncertainty of the sample mass ( $\pm 0.01$  g), and the uncertainty of the dissipated power in the sample ( $< 2\%$ ). This leads to the uncertainty of the measured specific heat capacity expressed by the error bars in **Figure 3a**. The specific heat capacity shows a temperature-independent value of  $c_p = (0.85 \pm 0.02)$  J g<sup>-1</sup> K<sup>-1</sup>, equivalent to a molar heat capacity of  $C_{m,p} = (46.49 \pm 1.15)$  J mol<sup>-1</sup> K<sup>-1</sup>. The given uncertainties are the confidence intervals for a confidence level of 95%. In **Figure 3b**, the total hemispherical emissivity  $\epsilon_{\text{tot}}$  is also presented, as obtained from measurement cycles in vacuum and Ar.

The measurement uncertainty of the total hemispherical emissivity is strongly dependent on the accuracy of determination of the external relaxation time  $\tau_1$ , which is better than 0.1 s. Furthermore, the sample radius and the measured heat capacity contribute to the measurement uncertainty. The last contribution is the used heat loss model. While in vacuum, heat loss is purely radiative, in Ar atmosphere, heat conduction, and radiation is taking place. The uncertainty of using an extended heat loss model<sup>[41]</sup> for the measurement in an Ar atmosphere has shown to deviate less than 1.4% from the measurements in vacuum. These factors are expressed by the error bars shown in **Figure 3b**. The total hemispherical emissivity is found to scatter around an average value of  $\epsilon_{\text{tot}} = 0.30 \pm 0.01$  (uncertainty is the standard deviation), which is higher than predicted from the theoretical approach by Parker and Abbott.<sup>[42]</sup>

The apparent thermal conductivity in the liquid phase, derived by the modulation calorimetry method presented earlier, is

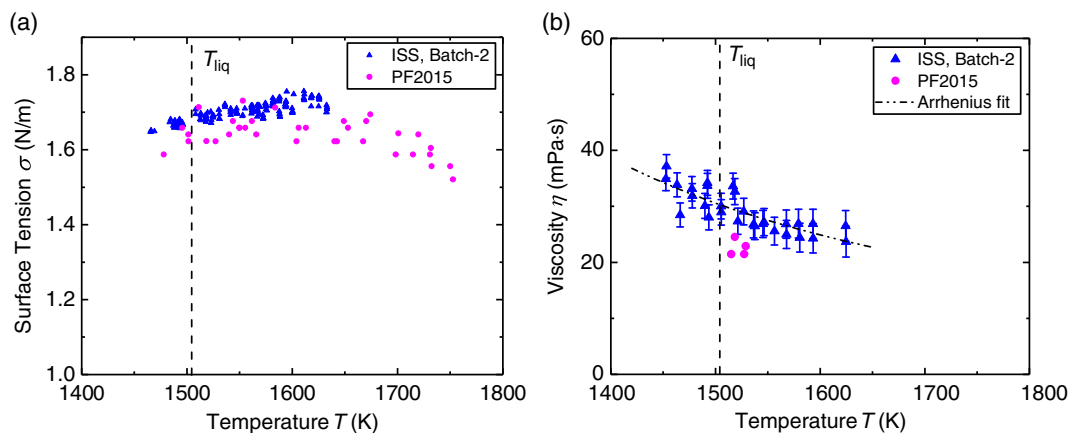


**Figure 2.** a) Surface tension as a function of temperature and b) Viscosity as a function of temperature, the dashed line is a fit using an Arrhenius equation.

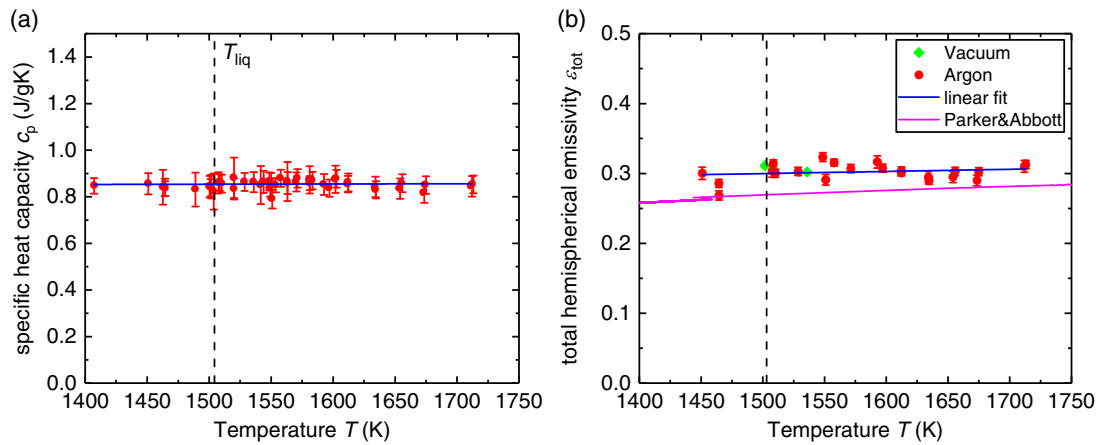


**Figure 3.** a) specific heat capacity of  $\text{Fe}_{57.75}\text{Ni}_{19.25}\text{Mo}_{10}\text{C}_5\text{B}_8$  in the liquid phase b) total hemispherical emissivity, measured (red circles—Ar, green square—vacuum), linearly fitted (blue line) and approximated using the equation of Parker and Abbott<sup>[42]</sup> (magenta line).

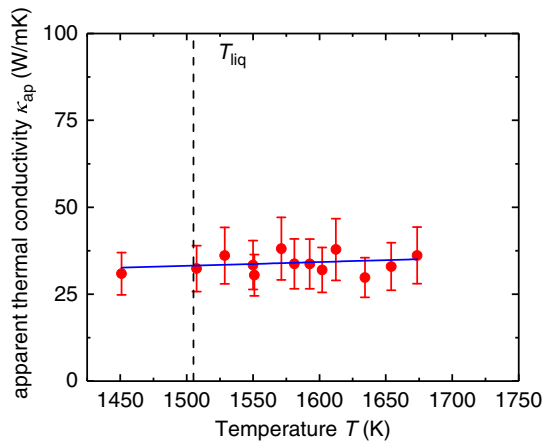


**Figure 4.** Apparent thermal conductivity of liquid  $\text{Fe}_{57.75}\text{Ni}_{19.25}\text{Mo}_{10}\text{C}_5\text{B}_8$ .

shown in **Figure 4**. For the analysis, the data points obtained with the faster modulation ( $f_{\text{mod}} = 0.30$  Hz) were used, as, under this condition, the measurement is farther from the adiabatic conditions and hence the derivation of the thermal conductivity is less prone to errors. Although given the limited number of data points, a slightly positive temperature coefficient is evident. The apparent thermal conductivity at the liquidus temperature is given as  $\kappa_{\text{ap}} = (32.4 \pm 6.6) \text{ W m}^{-1} \text{ K}^{-1}$ . The uncertainties of the measured thermal conductivity depend on the measurement uncertainty in sample radius and heat capacity, as well as on the time delay between the power excitation and the temperature response, which can be obtained with an accuracy of better than 0.01s. This translates to a measurement uncertainty  $\Delta\varphi$  of the phase shift as  $\Delta\varphi = 0.01s \cdot f_{\text{mod}} \cdot 360^\circ$ , which influences the accuracy of the determination of the internal relaxation time  $\tau_2$ . More importantly, the used modulation frequency plays a decisive role in error estimation. For the two used modulation frequencies (0.12 and 0.30 Hz), the higher frequency leads to a significant deviation of the phase angle from  $90^\circ$ , which leads to smaller influences of the uncertainty of the phase angle on the calculated internal relaxation time by Equation (6).

### 3.3. Electrical Resistivity and Mass Density

**Figure 5** shows the electrical resistivity in the solid and liquid phases, as obtained by the inductive measurement method. A strong discontinuity between the liquid and solid phase resistivities is obvious, signifying the crystallization of the sample during the cool-down.

The electrical resistivity in the liquid phase  $\rho_{e,l}$  exhibits a slightly negative slope, which even increases in magnitude with increasing temperature.

The electrical resistivity in the solid phase  $\rho_{e,s}$  can be described in the temperature range from 1200 to 1450 K as

$$\rho_{e,s} = (128.70 \pm 0.81) \mu\Omega \text{ cm} + (18.38 \pm 0.61) \times 10^{-3} \mu\Omega \text{ cm K}^{-1} \times T \quad (11)$$

and in the liquid phase, the electrical resistivity in the temperature range between 1600 and 1400 K can be described as

$$\rho_{e,l} = (163.65 \pm 0.68) \mu\Omega \text{ cm} - (1.69 \pm 0.44) \times 10^{-3} \mu\Omega \text{ cm K}^{-1} \times T \quad (12)$$

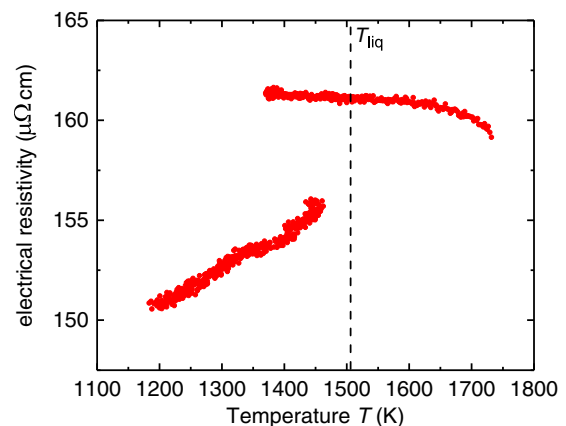


**Figure 5.** specific resistivity of  $\text{Fe}_{57.75}\text{Ni}_{19.25}\text{Mo}_{10}\text{C}_5\text{B}_8$ .

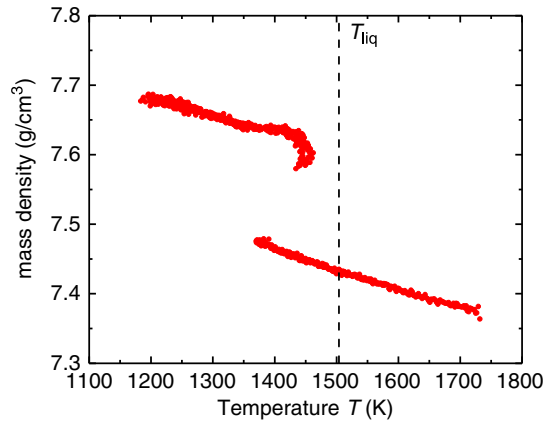


**Figure 6.** Mass density of  $\text{Fe}_{57.75}\text{Ni}_{19.25}\text{Mo}_{10}\text{C}_5\text{B}_8$  as a function of temperature in the liquid and high-temperature solid phase.

The given uncertainties in Equation (11) and (12) are the confidence interval for a confidence level of 95%.

In **Figure 6**, the mass density  $\rho_m$  as a function of temperature is shown for the solid and liquid phases, as derived from the radius measured by the inductive measurement method. The mass density in the high-temperature solid phase between 1150 and 1300 K can be described as

$$\rho_{m,s} = (8.00 \pm 0.03) \text{ g cm}^{-3} - (2.66 \pm 0.20) \times 10^{-4} \text{ g cm}^{-3} \text{ K}^{-1} \times T \quad (13)$$

and in the undercooled and stable liquid phase below 1700 K, the mass density can be expressed by

$$\rho_{m,l} = (7.83 \pm 0.02) \text{ g cm}^{-3} - (2.65 \pm 0.09) \times 10^{-4} \text{ g cm}^{-3} \text{ K}^{-1} \times T \quad (14)$$

Also in Equation (13) and (14), the given measurement uncertainties describe the confidence interval for a confidence level of 95%. **Table 1** shows a summary of the measured thermophysical properties of the alloy  $\text{Fe}_{57.75}\text{Ni}_{19.25}\text{Mo}_{10}\text{C}_5\text{B}_8$  (at%).

**Table 1.** Summary of the measured thermophysical properties of  $\text{Fe}_{57.75}\text{Ni}_{19.25}\text{Mo}_{10}\text{C}_5\text{B}_8$  (at%).

$T_{\text{liq}}$ [K]	1505 ± 4
$T_{\text{sol}}$ [K]	1325 ± 4
$\Delta H_f$ [J g <sup>-1</sup> ]	182 ± 10
$\sigma$ [N m <sup>-1</sup> ] at $T_{\text{liq}}$	1.68 ± 0.04
$\eta$ [mPa s] at $T_{\text{liq}}$	30 ± 3
$c_{p,l}$ [J g <sup>-1</sup> K <sup>-1</sup> ]	0.85 ± 0.02
$\epsilon_{\text{tot}}$	0.30 ± 0.01
$\kappa_{\text{ap}}$ [W m <sup>-1</sup> K <sup>-1</sup> ] at $T_{\text{liq}}$	32.4 ± 6.6
$\rho_{e,l}$ [μΩ cm] at $T_{\text{liq}}$	161.10 ± 0.68
$\rho_{m,l}$ [g cm <sup>-3</sup> ] at $T_{\text{liq}}$	7.43 ± 0.02 (extrapolated)
$\rho_{m,s}$ [g cm <sup>-3</sup> ] at $T_{\text{liq}}$	7.60 ± 0.03

## 4. Discussion

The surface tension of  $\text{Fe}_{57.75}\text{Ni}_{19.25}\text{Mo}_{10}\text{C}_5\text{B}_8$  measured in two independent experiments (on parabolic flight and on board the ISS) shows a boomerang-like shape, which is often attributed to the adsorption and desorption of surface-active species. As the oxygen partial pressure during both measurements was not measured, it is not conclusive, if the observed temperature dependence of the surface tension is inherent to the sample or an artifact of oxygen adsorption. The measured surface tension is below the surface tension of pure iron<sup>[43]</sup> and higher than that of the pure Fe–B system.<sup>[44]</sup> This can be rationalized by the also relatively high surface tension of nickel<sup>[43]</sup> and molybdenum.<sup>[45]</sup> In comparison with Zr-based metallic glasses,<sup>[46]</sup> the surface tension of  $\text{Fe}_{57.75}\text{Ni}_{19.25}\text{Mo}_{10}\text{C}_5\text{B}_8$  is about 5–10% higher.

It can be recognized, that the few viscosity values obtained during the parabolic flight are slightly smaller, but in general agreement with the measurements obtained on board the ISS. When comparing the viscosity at the liquidus temperature, the viscosity of  $\text{Fe}_{57.75}\text{Ni}_{19.25}\text{Mo}_{10}\text{C}_5\text{B}_8$  is much lower than for Zr-based metallic glasses.<sup>[41,46]</sup> Compared with pure iron,<sup>[47]</sup> the viscosity at the liquidus temperature of  $\text{Fe}_{57.75}\text{Ni}_{19.25}\text{Mo}_{10}\text{C}_5\text{B}_8$  is higher by at least a factor of 5.

The specific heat capacity shows no strong temperature dependence and is much higher ( $c_p = 0.85 \pm 0.02 \text{ J g}^{-1} \text{ K}^{-1}$  at  $T_{\text{liq}}$ ) than of Zr-based metallic glasses, such as, e.g., LM105 in the liquid ( $c_p = 0.56 \pm 0.01 \text{ J g}^{-1} \text{ K}^{-1}$  at  $T_{\text{liq}}$ <sup>[46]</sup>) and undercooled liquid phase,<sup>[48]</sup> or Vit106a.<sup>[49]</sup> At the same time,  $c_p$  of liquid  $\text{Fe}_{57.75}\text{Ni}_{19.25}\text{Mo}_{10}\text{C}_5\text{B}_8$  is higher than for pure liquid iron ( $c_p = 0.75 \text{ J g}^{-1} \text{ K}^{-1}$ <sup>[50]</sup>) but similar to other Fe-based metallic glasses in the liquid phase.<sup>[51]</sup>

The obtained total hemispherical emissivity value of  $\epsilon_{\text{tot}} = 0.30 \pm 0.01$  is similar to the values obtained for a titanium alloy<sup>[39]</sup> but higher than the values obtained for Ni-based superalloys.<sup>[52]</sup> The theoretical estimation of  $\epsilon_{\text{tot}}$  by Parker and Abbott is assuming the Drude free-electron model, however, under the assumption that the electronic relaxation time is negligibly small. Hence, details of the band structure and scattering mechanisms,<sup>[53]</sup> not considered by the simple prediction in the study by Parker and Abbott,<sup>[42]</sup> could explain the deviation of the measured total hemispherical emissivity from the model.

For the thermal conductivity of high-temperature liquid metallic melts, such as dealt with in this experiment, only a few measurement approaches exist.<sup>[54]</sup> Under the assumption that thermal transport is only due to electronic transport, the empirical Wiedemann–Franz law relates the product between the thermal conductivity  $\kappa$  and electrical resistivity  $\rho_e$ , to the temperature  $T$ :  $\kappa \cdot \rho_e = L \cdot T$ . The proportionality constant  $L$  is the theoretical Lorentz number,  $L = 2.45 \times 10^{-8} \text{ W } \Omega \text{ K}^{-2}$ . The thermal conductivity obtained in this way is  $\kappa = (22.9 \pm 0.1) \text{ W m}^{-1} \text{ K}^{-1}$  at the liquidus temperature, which is 29 % lower than the apparent thermal conductivity value of  $\kappa_{\text{ap}} = (32.4 \pm 6.6) \text{ W m}^{-1} \text{ K}^{-1}$  obtained by the modulation calorimetry method. The measured value is close to the thermal conductivity value for pure iron ( $\kappa = 36 \text{ W m}^{-1} \text{ K}^{-1}$ ) at the melting point.<sup>[47]</sup> The apparent thermal conductivity obtained by the modulation calorimetry method is generally a combination of the real thermal conductivity and the thermal conductivity contributed by the fluid flow. In our experiment, only small positioning forces had been applied

due to the microgravity environment, which drives only small convective flows inside the sample. Following the calculations presented in the studies by Xiao et al.,<sup>[55,56]</sup> the heater voltages applied during our modulation calorimetry experiments were small enough to ensure laminar flow throughout the whole experiment. The effect of laminar fluid flow patterns on the apparent thermal conductivity measured by the AC calorimetry method has been studied exemplarily on a Zr-based metallic glass sample measured during the MSL-1 mission.<sup>[57]</sup> It was shown that for small viscosities, the apparent thermal conductivity is generally overestimating the real thermal conductivity of the levitated liquid. Future studies are required to generalize these findings and to allow predictions of the influence on the thermal conductivity measured in this study.

A negative temperature coefficient of the electrical resistivity for disordered metals is often observed, and the observed temperature coefficient is in agreement with the empirical rule found by Mooij.<sup>[58]</sup> The temperature and composition dependence of the electrical resistivity of disordered and liquid alloys is often described in the framework of the Faber and Ziman theory.<sup>[59–64]</sup> The temperature has an influence on the radial distribution function and the Fermi vector  $k_F$ .<sup>[60,62,63,65]</sup> In the cases where the temperature coefficient is negative,  $2k_F$  is close to the first peak in the Fourier transform of the radial distribution function. At higher temperatures, the peaks in the Fourier transform of the radial distribution function become broader and hence, the total scattering is reduced, leading to a decrease in resistivity with an increase in temperature,<sup>[63]</sup> which can explain the decrease in specific resistivity observed for liquid  $\text{Fe}_{57.75}\text{Ni}_{19.25}\text{Mo}_{10}\text{C}_5\text{B}_8$  with increasing temperature. The density change between the liquid and solid state at  $T_{\text{liq}}$  is  $\Delta\rho_m = 0.17 \pm 0.02 \text{ g cm}^{-3}$ , which corresponds to a specific volume change of 2.28%. This is slightly smaller than the literature value of the specific volume change of pure iron at the melting point (3.46%).<sup>[66]</sup>

## 5. Conclusions

A large set of thermophysical properties in the liquid phase of a new Fe-based glass former,  $\text{Fe}_{57.75}\text{Ni}_{19.25}\text{Mo}_{10}\text{C}_5\text{B}_8$ , have been measured successfully using the electromagnetic levitator ISS-EML on board the International Space Station. The high-temperature data can now be used as input parameters for simulations and processing parameters for advanced manufacturing, including for powder production using gas atomization, surface coatings by laser cladding or spray coating, or for the fabrication of structural elements by additive manufacturing processes.

The  $\text{Fe}_{57.75}\text{Ni}_{19.25}\text{Mo}_{10}\text{C}_5\text{B}_8$  glass-forming alloy has a much higher liquidus temperature ( $T_{\text{liq}} = 1505 \text{ K}$ ) than Zr-based metallic glasses. The viscosity at  $T_{\text{liq}}$  is distinctly lower than at the liquidus temperature of Zr-based metallic glasses. This has important implications for the flow behavior of the melt during processing. The specific heat capacity in the liquid phase was shown to be much higher than the specific heat capacity of Zr-based metallic glasses, which is relevant when a certain cooling rate needs to be achieved during fabrication. The thermal conductivity was measured in two approaches, and it was shown that additional research has to be conducted to explain why the thermal conductivity obtained from the ac calorimetry is higher

than estimated by the electrical conductivity and the Wiedemann-Franz law. This work will hopefully be used in the future to develop processing parameters for a new class of tough and amorphous coatings and bulk parts for commercial applications.

## Acknowledgements

The authors acknowledge the access to the ISS-EML, which is a joint undertaking of the European Space Agency (ESA) and the DLR Space Administration. The reported work was conducted in the framework of the ESA MAP project ThermoProp (AO-099-022). We further acknowledge funding from the DLR Space Administration with funds provided by the Federal Ministry for Economic Affairs and Energy (BMWi) under Grant No. 50WM1759. DCH acknowledges support from NASA's Exploration Systems Mission Directorate under Contract no. NNN10ZTT001N. Part of this work was done at the Jet Propulsion Laboratory, California Institute of Technology, under contract with the National Aeronautics and Aerospace Administration. All authors are grateful to Dr. Rainer Wunderlich, Ulm University, and Prof. Livio Battezzati, Università di Torino, for fruitful discussions and technical support.

## Conflict of Interest

The authors declare no conflict of interest.

## Keywords

iron-based metallic glasses, specific heat, surface tension, thermal conductivity, total hemispherical emissivity, viscosity

Received: September 23, 2020

Revised: October 26, 2020

Published online:

- [1] M. F. Ashby, A. L. Greer, *Scr. Mater.* **2006**, *54*, 321.
- [2] A. Peker, W. L. Johnson, *Appl. Phys. Lett.* **1993**, *63*, 2342.
- [3] C. Suryanarayana, A. Inoue, *Int. Mater. Rev.* **2013**, *58*, 131.
- [4] G. Y. Koga, A. M. Jorge Junior, V. Roche, R. P. Nogueira, R. Schulz, S. Savoie, A. K. Melle, C. Loable, C. Bolfarini, C. S. Kiminami, W. J. Botta, *Metall. Mater. Trans. A Phys. Metall. Mater. Sci.* **2018**, *49*, 4860.
- [5] T. Paul, S. H. Alavi, S. Biswas, S. P. Harimkar, *Lasers Manuf. Mater. Process.* **2015**, *2*, 231.
- [6] G. Telasang, J. Dutta Majumdar, G. Padmanabham, M. Tak, I. Manna, *Surf. Coatings Technol.* **2014**, *258*, 1108.
- [7] A. Inoue, B. L. Shen, A. R. Yavari, A. L. Greer, *J. Mater. Res.* **2003**, *18*, 1487.
- [8] V. Ponnambalam, S. J. Poon, G. J. Shiflet, *J. Mater. Res.* **2004**, *19*, 3046.
- [9] X. J. Gu, S. J. Poon, G. J. Shiflet, M. Widom, *Appl. Phys. Lett.* **2008**, *92*, 10.
- [10] M. E. Launey, D. C. Hofmann, J. Y. Suh, H. Kozachkov, W. L. Johnson, R. O. Ritchie, *Appl. Phys. Lett.* **2009**, *94*, 31.
- [11] D. C. Hofmann, J. Y. Suh, A. Wiest, G. Duan, M. L. Lind, M. D. Demetriou, W. L. Johnson, *Nature* **2008**, *451*, 1085.
- [12] P. Gargarella, A. Almeida, R. Vilar, C. R. M. Afonso, S. Peripolli, C. T. Rios, C. Bolfarini, W. J. Botta, C. S. Kiminami, *Surf. Coat. Technol.* **2014**, *240*, 336.
- [13] Y. Y. Zhu, Z. G. Li, R. F. Li, M. Li, X. L. Daze, K. Feng, Y. X. Wu, *Appl. Surf. Sci.* **2013**, *280*, 50.



- [14] P. Bordeenithikasem, D. C. Hofmann, S. Firdosy, N. Ury, E. Vogli, D. R. East, *J. Alloys Compd.* **2020**, 157537.
- [15] D. C. Hofmann, P. Bordeenithikasem, A. Pate, S. N. Roberts, E. Vogli, *Adv. Eng. Mater.* **2018**, 20, 1.
- [16] A. Bandyopadhyay, K. D. Traxel, *Addit. Manuf.* **2018**, 22, 758.
- [17] A. Kout, T. Wiederkehr, H. Müller, *Surf. Coat. Technol.* **2009**, 203, 1580.
- [18] H. Tian, X. Chen, Z. Yan, X. Zhi, Q. Yang, Z. Yuan, *Appl. Phys. A Mater. Sci. Process.* **2019**, 125, 1.
- [19] Q. Chai, C. Fang, J. Hu, Y. Xing, D. Huang, *Mater. Des.* **2020**, 195, 109033.
- [20] M. Pasandideh-Fard, V. Pershin, S. Chandra, J. Mostaghimi, *J. Therm. Spray Technol.* **2002**, 11, 206.
- [21] M. Wei, S. Chen, M. Sun, J. Liang, C. Liu, M. Wang, *Powder Technol.* **2020**, 367, 724.
- [22] K. Hanthanan Arachchilage, M. Haghshenas, S. Park, L. Zhou, Y. Sohn, B. McWilliams, K. Cho, R. Kumar, *Adv. Powder Technol.* **2019**, 30, 2726.
- [23] I. Egry, H. Giffard, S. Schneider, *Meas. Sci. Technol.* **2005**, 16, 426.
- [24] S. Sauerland, K. Eckler, I. Egry, *J. Mater. Sci. Lett.* **1992**, 11, 330.
- [25] K. Eckler, I. Egry, D. M. Herlach, *Mater. Sci. Eng. A* **1991**, 133, 718.
- [26] I. Egry, *J. Mater. Sci.* **1991**, 26, 2997.
- [27] M. Mohr, R. K. Wunderlich, K. Zweiaccker, S. Prades-Rödel, R. Sauguet, A. Blatter, R. Logé, A. Neels, W. L. Johnson, H. J. Fecht, *Nat. Microgravity* **2019**, 5, 4.
- [28] B. Glaubnitz, K. Kullack, W. Dreier, A. Seidel, W. Soellner, A. Diefenbach, S. Schneider, in *Deutsche Medizinische Wochenschrift* **2015**, p. 1.
- [29] G. Lohöfer, J. Piller, G. Lohoefer, J. Piller, in *40th AIAA Aerospace Sciences Meeting and Exhibition*, American Institute of Aeronautics and Astronautics, Reston, VA **2002**.
- [30] A. Seidel, W. Soellner, C. Stenzel, *J. Phys. Conf. Ser.* **2011**, 327, 012015.
- [31] X. Xiao, R. W. Hyers, R. K. Wunderlich, H. J. Fecht, D. M. Matson, *Appl. Phys. Lett.* **2018**, 113, 11903.
- [32] M. Mohr, R. K. Wunderlich, S. Koch, P. K. Galenko, A. K. Gangopadhyay, K. F. Kelton, J. Z. Jiang, H.-J. Fecht, *Microgravity Sci. Technol.* **2019**, 31, 177.
- [33] F. R. S. Rayleigh, *Proc. R. Soc.* **1879**, 29, 71.
- [34] H. Lamb, *Proc. Lond. Math. Soc.* **1881**, 13.
- [35] H. J. Fecht, W. L. Johnson, *Rev. Sci. Instrum.* **1991**, 62, 1299.
- [36] R. K. Wunderlich, D. S. Lee, W. L. Johnson, H.-J. Fecht, *Phys. Rev. B – Condens. Matter Mater. Phys.* **1997**, 55, 26.
- [37] R. K. Wunderlich, *Adv. Eng. Mater.* **2001**, 3, 924.
- [38] R. K. Wunderlich, H.-J. Fecht, *Meas. Sci. Technol.* **2005**, 16, 402.
- [39] M. Mohr, R. Wunderlich, R. Novakovic, E. Ricci, H. J. Fecht, *Adv. Eng. Mater.* **2020**, 22, 2000169.
- [40] G. Lohöfer, *Rev. Sci. Instrum.* **2018**, 89, 124709.
- [41] Z. Evenson, T. Schmitt, M. Nicola, I. Gallino, R. Busch, *Acta Mater.* **2012**, 60, 4712.
- [42] W. J. Parker, G. L. Abbott, in *Symp. Thermal Radiation of Solids* (Ed: S. Katzoff), Scientific and Technical Information Division, National Aeronautics and Space Administration, Washington, DC **1964**, p. 11.
- [43] J. Brillo, I. Egry, *J. Mater. Sci.* **2005**, 40, 2213.
- [44] M. Tomut, H. Chiriac, M. Marinescu, F. Necula, *J. Non. Cryst. Solids* **1999**, 250–252, 655.
- [45] P. F. Paradis, T. Ishikawa, N. Koike, *Int. J. Refract. Met. Hard Mater.* **2007**, 25, 95.
- [46] M. Mohr, R. K. Wunderlich, D. C. Hofmann, H.-J. Fecht, *Npj Microgravity* **2019**, 5, 24.
- [47] K. C. Mills, *Recommended Values of Thermophysical Properties for Selected Commercial Alloys*, Woodhead Publishing Limited, Cambridge **2002**.
- [48] S. C. Glade, R. Busch, D. S. Lee, W. L. Johnson, R. K. Wunderlich, H. J. Fecht, *J. Appl. Phys.* **2000**, 87, 7242.
- [49] I. Gallino, M. B. Shah, R. Busch, *J. Alloys Compd.* **2007**, 434–435, 141.
- [50] K. C. Mills, Y. M. Youssef, Z. Li, Y. Su, *ISIJ Int.* **2006**, 46, 623.
- [51] A. Castellero, G. Fiore, N. Van Steenberge, L. Battezzati, *J. Alloys Compd.* **2020**, 843, 156061.
- [52] M. Mohr, R. Wunderlich, Y. Dong, D. Furrer, H.-J. Fecht, *Adv. Eng. Mater.* **2020**, 22, 1901228.
- [53] A. J. Sievers, *J. Opt. Soc. Am.* **1978**, 68, 1505.
- [54] P. Pichler, G. Pottlacher, *Impact of Thermal Conductivity on Energy Technologies*, InTech, London **2018**, p. 38.
- [55] X. Xiao, R. W. Hyers, D. M. Matson, *Int. J. Heat Mass Transf.* **2019**, 136, 531.
- [56] X. Xiao, J. Lee, R. W. Hyers, D. M. Matson, *Npj Microgravity* **2019**, 5, 7.
- [57] X. Ye, *A Computational Study on Extension of Non-Contact Modulation Calorimetry*, University of Massachusetts – Amherst, **2015**.
- [58] J. H. Mooij, *Phys. Status Solidi* **1973**, 17, 521.
- [59] J. M. Ziman, *Philos. Mag.* **1961**, 6, 1013.
- [60] C. C. Bradley, T. E. Faber, E. G. Wilson, J. M. Ziman, *Philos. Mag.* **1962**, 7, 865.
- [61] T. E. Faber, J. M. Ziman, *Philos. Mag.* **1965**, 11, 153.
- [62] O. Dreirach, R. Evans, H. J. Guntherodt, H. U. Kunzi, *J. Phys. F Met. Phys.* **1972**, 2, 709.
- [63] H. J. Guntherodt, E. Hauser, H. U. Kunzi, R. Evans, J. Evers, E. Kaldis, *J. Phys. F Met. Phys.* **1976**, 6, 1513.
- [64] R. Evans, H.-J. Güntherodt, H. U. Kunzi, A. Zimmermann, *Phys. Lett.* **1972**, 38A, 151.
- [65] G. Busch, H. J. Güntherodt, *Phys. Der Kondens. Mater.* **1967**, 6, 325.
- [66] J. Blumm, J. B. Henderson, *High Temp. – High Press.* **2000**, 32, 109.